ACS OMEGA

http://pubs.acs.org/journal/acsodf

Article

Quantitative Measurement of OH* and CH* Chemiluminescence in Jet Diffusion Flames

Yao Liu, Jianguo Tan,* Minggang Wan, Lang Zhang, and Xiao Yao

Cite This: ACS Omega 2020, 5, 15922−15930

Read Online

ACCESS | Metrics & More | Article Recommendations

ABSTRACT: Quantitative measurement of chemiluminescence is a challenging work that limits the development of combustion diagnostics based on chemiluminescence. Here, we present a feasible method to obtain effective quantitative chemiluminescence data with an integrating sphere uniform light source. Spatial distribution images of OH* and CH* radiation from methane laminar diffusion flames were acquired using intensified charge-coupled device (CCD) cameras coupled with multiple lenses and narrow-band-pass filters. After the process of eliminating background emissions by three filters and the Abel inverse transformation, the chemiluminescence intensity was converted to a radiating rate based on the uniform light source. The simulated distributions of OH* and CH* agree well with the experimental results. It has also been found that the distribution of OH* is more extensive and closer to the flame front than that of CH*, demonstrating that OH* is more representative of the flame structure. Based on the change in the reaction rate of different formation reactions, OH* distributions can be divided into three regions: intense section near the nozzle, transition section in the middle of the flame, and secondary section downstream the flame, whereas CH* only exists in the first two regions. In addition, as the velocity ratio of methane and co-flowing air increases, the main reactions become more intense, while the secondary reaction of OH* becomes weaker.

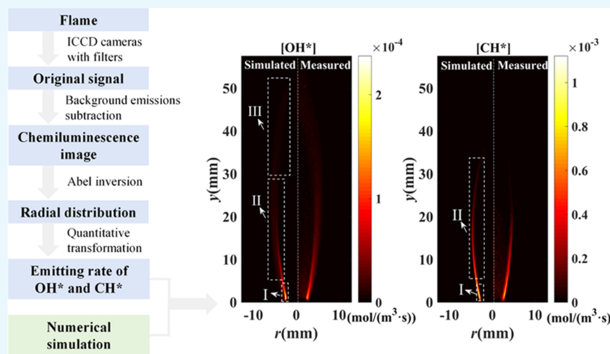

1. INTRODUCTION

Chemiluminescence in flames refers to the spontaneous light emissions from chemically excited species by an electronic exchange process.[1] The generation of chemiluminescence mainly includes two steps: the formation (R1) and the radiative transition (R2) of excited-state radicals. It is important to highlight that not all excited-state radicals are involved in the process of generating chemiluminescence. As shown in reaction R3, some of them collide or react with other species, causing nonradiative transitions

$$A + B \rightarrow R^* + \text{ others} \quad \text{(R1)}$$

$$R^* \rightarrow R + h\nu \quad \text{(R2)}$$

$$R^* + M \rightarrow R + M \quad \text{(R3)}$$

where A, B, and R are different ground-state radicals; R* is an excited-state radical; and M is a third body species.

Since chemiluminescence imaging can provide much useful information including the combustion state,[2,3] the location of the reaction zone,[3−7] the equivalence ratio,[8−13] and the heat release rate,[14−20] it has been widely used in research and industrial combustor control. For the flames of hydrocarbons, OH* and CH* are the most important excited-state radicals, with peak wavelengths of 308 and 431 nm, respectively. He et al.[3] investigated the laminar methane−oxygen co-flow diffusion flames and found that OH* chemiluminescence under different equivalence ratios can indicate the combustion state, such as being oxygen-deficient or oxygen-enriched. Deleo et al.[7] obtained the spatial distributions of OH* and CH* in opposed flow diffusion methane flames, which showed that both OH* and CH* radicals are generated in the reaction region, and the peak intensities are good indicators of the methane flame fronts. Moreover, Quintino et al.[8] numerically and experimentally studied CH_4/CO_2/air flames with different equivalence ratios. It was concluded that the equivalence ratio of the tested blends can be inferred from OH*/CH*, OH*/C_2*, and CH*/C_2*. In addition, many researchers have realized three-dimensional flame imaging through computed tomography of chemiluminescence (CTC).[21−30] In particular, Cai et al.[21−27] introduced various imaging instruments into the CTC, including fiber bundles, reflective mirrors, plenoptic cameras, and single-pixel cameras. Diverse reconstruction

Received: March 11, 2020
Accepted: June 8, 2020
Published: June 25, 2020

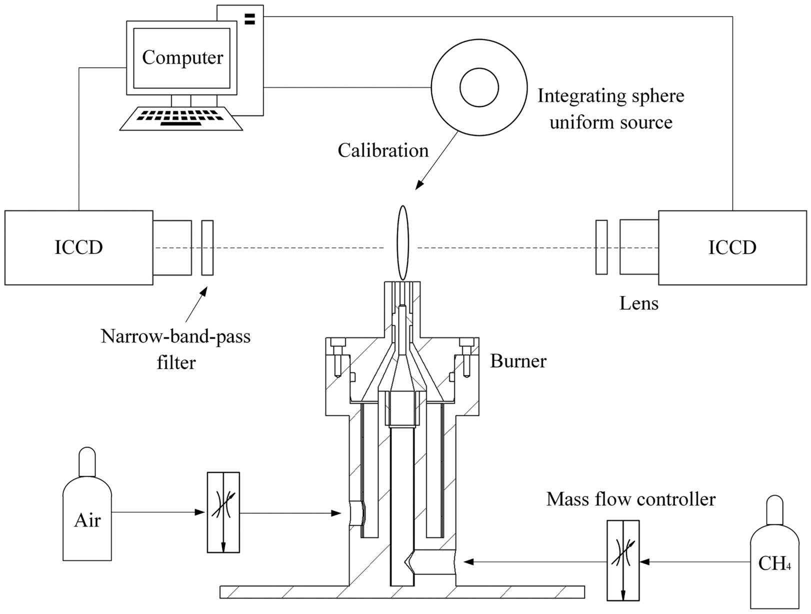

Figure 1. Sketch of the experimental setup.

algorithms are also applied in their works, such as algebraic reconstruction technique, proper orthogonal decomposition, and deep leaning.

However, most of the previous research studies are limited to qualitative chemiluminescence imaging and hardly quantify the excited radicals, while the quantitative comparison of results for OH* and CH* is important in chemiluminescence studies and is indispensable for the verification of modeling. The chemiluminescence intensities could be converted into meaningful concentrations to some extent using Raman and Rayleigh scattering,[31−34] whereas they feature complicated systems and a clear measurement environment. At the same time, the combustion environment tends to be more and more harsh, and thus, these two expensive methods are difficult to be conducted in practical applications. To find an alternative diagnostic technique of quantitative chemiluminescence, Zhao et al.[1] determined local concentrations of an OH* radical via a light source of known radiance in a hydrogen diffusion flame. However, they failed to take into account the effects of nonradiative transitions of OH*. It is noteworthy that Wang et al.[35] introduced a Monte Carlo tracing of photons to correct the optical paths of a CH_4/air plane premixed flame, and the wavelength responsivity of the optical detection system was calibrated using a quartz tungsten halogen lamp. They found that the concentration distributions of CH*, OH*, C_2*, and CO_2* are consistent with simulation results, but this method only works for one-dimensional plane flames.

The novelty of the current study is to propose a simple method to obtain quantitative emitting data of excited radicals based on an integrating sphere uniform light source, which is suitable for axisymmetric flames. With the ground-state reaction mechanism GRI-Mech 3.0 as well as generation and consumption reactions of OH* and CH*, numerical simulation was carried out to be compared with the experimental measurements. In addition, the distribution characteristics of OH* and CH* chemiluminescence were obtained, and the influence of gas velocity ratio (k_u) on the radiation characteristics was investigated.

2. EXPERIMENTAL STUDY

2.1. Combustion System and Operating Conditions.

Figure 1 shows the schematic of the experimental setup consisting of a jet diffusion burner and the associated instruments. The burner was designed to generate stabilized laminar axisymmetric flames. In the burner center was a coaxial two-channel non-premixed nozzle with a central channel inner diameter of 2 mm and an outer diameter of 4 mm. The inner and outer diameters of the external jet nozzle are 6 and 21 mm, respectively, which form an annular coaxial channel with the outer wall of the central nozzle. Pure methane was used as fuel and pumped through the central channel, and the oxidizer air went through the external annulus to the outlet of the nozzle, where it was mixed with the fuel. Moreover, the mass flow of methane and air was measured and adjusted by different mass flow controllers (Sevenstar CS200 and CS230).

In this work, $k_u = u_{air}/u_{CH_4}$, where u_{air} represents the velocity of external airflow and u_{CH_4} represents the velocity of central methane flow. Table 1 reports the five cases designed to study the effects of k_u on the flame. The volume flow rates of methane and air are respectively denoted by V_{CH_4} and V_{air}.

Table 1. Operating Conditions in This Study

case	u_{CH_4} (m/s)	u_{air} (m/s)	V_{CH_4} (L/min)	V_{air} (L/min)	k_u
1	1.0	0.2	0.1885	3.817	0.2
2	1.0	0.4	0.1885	7.634	0.4
3	1.0	0.6	0.1885	11.451	0.6
4	1.0	0.8	0.1885	15.268	0.8
5	1.0	1.0	0.1885	19.085	1.0

2.2. Chemiluminescence Measurements.

The chemiluminescence imaging system is mainly composed of two intensified charge-coupled device (ICCD) cameras with 1024 × 1024 pixels, 10 nm narrow-band-pass filters, an integrating sphere uniform light source, lenses, and a computer, as shown in Figure 1. In the experiment, the two cameras were symmetrically placed on both sides of the flame and

https://dx.doi.org/10.1021/acsomega.0c01093
ACS Omega 2020, 5, 15922−15930

synchronized at an acquisition frequency of 8 fps, with an exposure time of 2 ms and an aperture of 5.6.

For OH* and CH* chemiluminescence, different filters were fixed between the flame and lens to eliminate interference from other emissions so that the images could be obtained at specified wavelength ranges. The filters used in this work are listed in Table 2.

Table 2. Filters Used in This Work

excited-state radicals	brand	central wavelength (nm)	transmittance at central wavelength (%)	full width at half-maximum (nm)
OH*	Edmund 34980	310	70	10
CH*	Edmund 65197	420	85	10
	Edmund 65198	430	85	10
	Edmund 65200	442	85	10

The OH* chemiluminescence image was acquired with a UV quartz lens and a 10 nm narrow-band-pass filter with a central wavelength at 310 nm since the OH* radiation mainly exists in the UV region from 280 to 350 nm with a peak at 308 nm. According to previous studies,[1,12] emissions due to other species (mainly associated with CO_2*) are comparatively weak in the UV region, about 3.5% of the OH* radiation intensity.

In contrast, the CH* radiation exists in the visible region (380−760 nm) with intense background emissions, including soot radiation and CO_2*. There are both background light and CH* chemiluminescence in the shooting result of the 430 nm filter of CH*, so it is necessary to eliminate the influence of background emissions. Referring to the processing method proposed by Karnani,[36] as there are only background emissions in the images taken by filters centered at 420 and 442 nm, the two can be used to estimate background emissions at 430 nm.

The customized integrating sphere uniform light source from Labsphere Inc. was for calibration of the imaging system. Inside the integrating sphere, there are several UV LEDs with a wavelength of 308 and 431 nm, respectively, so that it can emit light at the same wavelength as OH* and CH* chemiluminescence. As the irradiance of the uniform light is adjustable and the uniformity can reach 99%, the radiating rate of OH* and CH* can be obtained through comparison with the uniform light, which will be described in detail in Section 2.3. It is worth noting that when shooting the uniform light source, it was positioned at the identical object distance as that of the burner as shown in Figure 1, and the various settings of the cameras mentioned above should also remain the same.

2.3. Processing of Chemiluminescence Images. As the geometry of the burner is not perfectly axisymmetric and there may be a possible slight movement of the flames in the experimental measurement, the flame images acquired by ICCD were not perfectly axisymmetric. To eliminate the asymmetry and reduce the noise in the raw signals, 50 images of OH* and CH* were separately captured and then averaged under each case. The average images were then smoothed with a 10-pixel moving average filter.

In addition, for CH* chemiluminescence, the contributions of background emissions, including soot and CO_2*, have to be subtracted from the images at 430 nm. It is assumed that the soot emissions come from radiation of an ideal blackbody. According to Planck's law

$$I_{\lambda,T}^{\text{soot}} = \frac{2hc^2}{\lambda^5}\frac{1}{e^{hc/\lambda k_b T} - 1} \tag{1}$$

where $I_{\lambda,T}^{\text{soot}}$ is the soot radiation intensity at a given wavelength, T is the absolute temperature, h is the Planck constant, c is the speed of light, λ is the wavelength of the light, and k_b is the Boltzmann constant. Since the actual temperature of soot particles is too difficult to measure, the background radiation at 430 nm cannot be calculated directly. As mentioned above, the background emissions at 430 nm can be estimated between those measured at 420 and 442 nm, as the following equation

$$\begin{aligned}&\int I_{\lambda,T}^{\text{soot}}\cdot \text{Tr}_{430\text{ nm}}(\lambda)\\ &= a\cdot\int I_{\lambda,T}^{\text{soot}}\cdot \text{Tr}_{420\text{ nm}}(\lambda) + b\cdot\int I_{\lambda,T}^{\text{soot}}\cdot \text{Tr}_{442\text{ nm}}(\lambda)\end{aligned} \tag{2}$$

where a and b are the coefficients associated with the imaging system, and Tr is the transmission of the filters.

Suppose if T_1 = 1800 K and T_2 = 2000 K,[13] then, two sets of intensity data at 420, 430, and 442 nm can be obtained by eq 1, respectively. Substituting these two sets of data into eq 2, we can get a = 0.7212 and b = 0.3317. To further simplify the computation, let $I_{\lambda,T}^{\text{soot}}$ be the soot radiation intensity obtained by the ICCD camera with the corresponding filter. Thus, eq 2 can be simplified to

$$I_{430\text{ nm}}^{\text{soot}} = 0.7212 I_{420\text{ nm}}^{\text{soot}} + 0.3317 I_{442\text{ nm}}^{\text{soot}} \tag{3}$$

From the study of Zhang,[13] we can know that the CO_2* emission intensity remains nearly unchanged in the wavelength range from 410 to 450 nm, namely, $I_{430\text{ nm}}^{CO_2*} = I_{420\text{ nm}}^{CO_2*} = I_{442\text{ nm}}^{CO_2*}$. Therefore, eq 3 could also be used to evaluate the CO_2* emission at 430 nm

$$0.7212 I_{420\text{ nm}}^{CO_2*} + 0.3317 I_{442\text{ nm}}^{CO_2*} = 1.0529 I_{430\text{ nm}}^{CO_2*} \approx I_{430\text{ nm}}^{CO_2*} \tag{4}$$

The error of the CO_2* contribution calculated from this equation is 5.29%. Then, from eq 5, a generic equation for eliminating soot and CO_2* emissions could be obtained

$$\begin{aligned}I_{CH*} &= I_{430\text{ nm}}^{\text{total}} - (I_{430\text{ nm}}^{\text{soot}} + I_{430\text{ nm}}^{CO_2*})\\ &\approx I_{430\text{ nm}}^{\text{total}} - (0.7212 I_{420\text{ nm}}^{\text{total}} + 0.3317 I_{442\text{ nm}}^{\text{total}})\end{aligned} \tag{5}$$

where $I_{\lambda}^{\text{total}}$ is the radiation intensity measured by the ICCD camera with the corresponding filter.

Taking case 4 for example, the subtraction procedure diagram of CH* chemiluminescence images is shown in Figure 2.

Furthermore, the images captured by the camera is the projection along the line of sight, which is not conducive to direct analysis. Therefore, the results processed above were transformed from line-of-sight-integrated images to two-dimensional radial distributions, through a three-point Abel inversion method.[37]

2.4. Quantitative Transformation. After the radial distribution of chemiluminescence being obtained, the integrating sphere uniform light source was used to estimate the quantitative emitting data of the excited radicals. With the same imaging system, the light intensity is considered to be proportional to the number of luminous particles. Within the same pixel, therefore, the ratio of the intensity of Abel inverted

https://dx.doi.org/10.1021/acsomega.0c01093
ACS Omega 2020, 5, 15922−15930

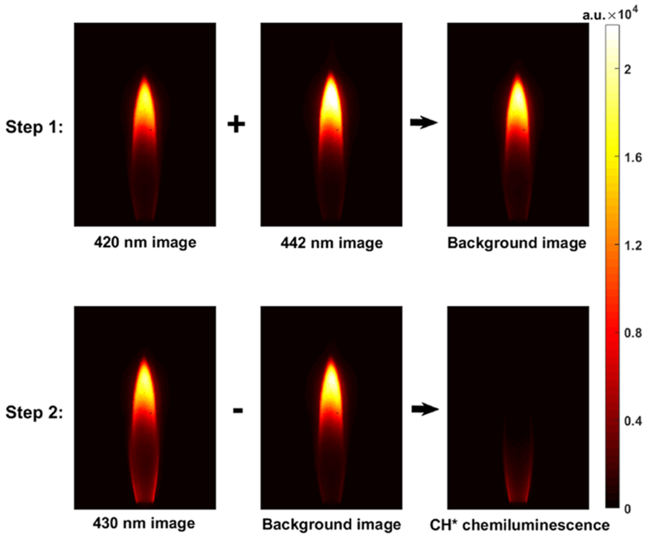

Figure 2. Subtraction procedure of background emissions in CH* chemiluminescence.

OH* chemiluminescence ($I_{OH*,Abel}$) and light source (I_c) is equal to the ratio of the number of photons emitted by OH* chemiluminescence (N_{OH*}) and from the calibration light source (N_c)[1]

$$\frac{I_{OH*,Abel}}{I_c} = \frac{N_{OH*}}{N_c} \tag{6}$$

The right side of eq 6 can be obtained by

$$\frac{N_{OH*}}{N_c} = \frac{\frac{1}{4\pi}[OH^*]N_A\eta_{308\ nm}\tau\Delta t}{\int_{\lambda=305}^{315}\frac{S_{c(\lambda)}}{h\nu}\eta_\lambda d\lambda\tau\Delta t} \tag{7}$$

where [OH*] ($mol\cdot m^{-3}\cdot s^{-1}$) is the mole of OH* emitting photons per second and in unit volume, namely, the emitting rate of OH*. N_A is the Avogadro constant, and $\eta_{308\ nm}$ is the transmittance of a 34980 filter at 308 nm, which is equal to 57.4% in this paper. τ is the efficiency of the collection optics, and Δt (s) is the exposure time of the ICCD camera. $S_{c(\lambda)}$ is the irradiance of the light source related to the wavelength λ, which is equal to 5×10^{-2} $w/(m^2\cdot\mu m\cdot sr)$ at 308 nm in this work, and $h\nu$ is the photon energy.

Thus, the emitting rate of OH* can be expressed as eq 7.

$$[OH^*] = \frac{4\pi I_{OH*,Abel}}{I_c\eta_{308\ nm}}\int_{\lambda=305}^{315}\frac{S_{c(\lambda)}}{h\nu}\eta_\lambda d\lambda \tag{8}$$

It is worth noting that compared to the overall fractional transmission,[1] the simplified transmittance $\eta_{308\ nm}$ will introduce an error of less than 4%. The CH* data were processed with the same procedures. At this point, the quantitative transformation of OH* and CH* from light intensity to the emitting rate has been completed.

3. NUMERICAL METHOD

3.1. Chemical Reaction Mechanisms. The numerical simulation was conducted based on the study of He et al.[3] and Hu et al.[19] Ground-state radicals are the source of excited-state species, and the most widely used version of ground-state chemical reactions is GRI-Mech 3.0, which contains 53 species and 325 elementary reactions. However, due to the limitation of the Fluent used in this work, mechanisms as complex as GRI-Mech 3.0 are not applicable. Therefore, all of the nitrogen-related species had been removed, except N_2.

Moreover, the chemical reaction mechanisms listed in Table 3 were added to model the formation and quenching of OH* and CH*. In the table, A is a pre-exponential factor, T is the temperature, b is the temperature exponent, E is the activation energy, and R is the universal gas constant. As mentioned in Section 1, only reactions R6 and R16 are engaged in the generation of chemiluminescence, while reactions R7−R15 and R17−R23 are the nonradiative transitions of OH* and CH*, respectively. In total, 37 species and 237 reactions constituted the adopted reaction model.

3.2. Numerical Model. Figure 3 illustrates a 2D axisymmetric computational domain corresponding to the

Table 3. Chemical Reactions of OH* and CH*

no.	reaction	A ($cm^3/mol\cdot s$)	b	E (cal/mol)	ref
R4	$CH + O_2 = CO + OH^*$	4.82×10^{10}	0.0	167	38
R5	$H + O + M = OH^* + M$	5.45×10^{12}	0.0	0	38
R6	$OH^* \rightarrow OH + h\nu$	1.45×10^{6}	0.0	0	39
R7	$OH^* + N_2 = OH + N_2$	1.08×10^{11}	0.5	−1238	39
R8	$OH^* + O_2 = OH + O_2$	2.10×10^{12}	0.5	−482	39
R9	$OH^* + H_2O = OH + H_2O$	5.92×10^{12}	0.5	−861	39
R10	$OH^* + H_2 = OH + H_2$	2.95×10^{12}	0.5	−444	39
R11	$OH^* + CO_2 = OH + CO_2$	2.75×10^{12}	0.5	−968	40
R12	$OH^* + CO = OH + CO$	3.23×10^{12}	0.5	−787	40
R13	$OH^* + CH_4 = OH + CH_4$	3.36×10^{12}	0.5	−635	39
R14	$C_2H + O_2 = CO_2 + CH^*$	6.02×10^{-4}	4.4	−2285	39
R15	$C_2H + O = CO + CH^*$	6.02×10^{12}	0.0	457	38
R16	$CH^* \rightarrow CH + h\nu$	1.85×10^{6}	0.0	0	39
R17	$CH^* + N_2 = CH + N_2$	3.03×10^{2}	3.4	−381	39
R18	$CH^* + O_2 = CH + O_2$	2.48×10^{6}	2.1	−1720	39
R19	$CH^* + H_2O = CH + H_2O$	5.30×10^{13}	0.0	0	39
R20	$CH^* + H_2 = CH + H_2$	1.47×10^{14}	0.0	1361	39
R21	$CH^* + CO_2 = CH + CO_2$	2.40×10^{-1}	4.3	−1694	39
R22	$CH^* + CO = CH + CO$	2.44×10^{12}	0.5	0	39
R23	$CH^* + CH_4 = CH + CH_4$	1.73×10^{13}	0.0	167	39

https://dx.doi.org/10.1021/acsomega.0c01093
ACS Omega 2020, 5, 15922−15930

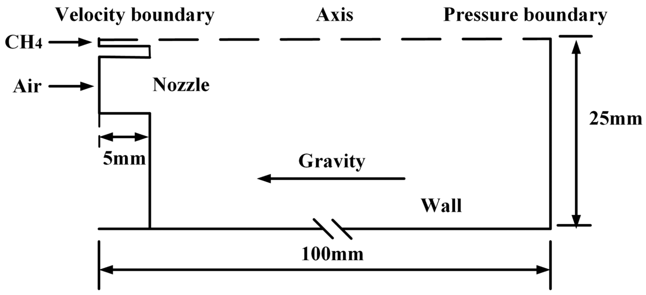

Figure 3. Computational domain and boundary conditions.

diffusion burner. The computational domain has an axial length of 100 mm and a radial length of 25 mm. The 5 mm burner height is to consider the preheating of fuels and the velocity distributions at the nozzle outlet. The radial dimensions of the computational domain are the same as the actual one, with methane flowing in the central channel and air in the annular coaxial channel. To ensure the accuracy of the simulation results, a structured mesh with about 620 000 cells was used after a grid independence study. Boundary conditions at the gas inlets were all set to the velocity boundary, the lower boundary and the left boundary except the nozzle part were set as the wall, and the upper boundary was set as the symmetry axis. Pressure boundary was used for the outlet, with the pressure setting as the standard ambient conditions.

It should be noted that there are gaseous molecules in the methane flame causing radiative heat loss, including CH_4, CO_2, CO, and H_2O. Considering their effects, the discrete ordinates (DO) radiation model was adopted as it spanned the entire range of optical thickness. The weighted-sum-of-gray-gases model (WSGGM) was used to calculate the absorption coefficient of a gas mixture. In addition, multicomponent diffusion and thermal diffusion were considered in the modeling.

4. RESULTS AND DISCUSSION

4.1. Results of the Quantitative Measurement. Figures 4 and 5 show a comparison of the quantitative measurements of OH* and CH* radiation with the simulated results (case 2). It is important to point out that the measured results of OH* and CH* are only compared with reactions R6 and R16, respectively, as the other reactions are the nonradiative transitions of the two excited-state radicals.

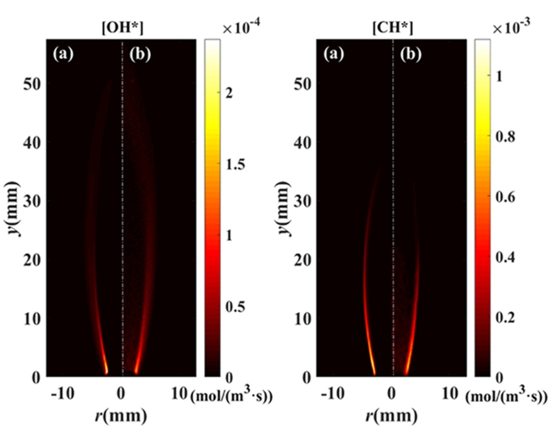

Figure 4. Profiles of [OH*] and [CH*] obtained by (a) numerical simulation and (b) quantitative measurement (case 2), where r is the radial position and y is the axial height from the burner.

From the overall profiles plotted in Figure 4, we can see that the numerically simulated emission intensities of OH* and CH* are within the same order of magnitude as the experimental values. In addition, the measured and simulated distributions of the OH* emitting rate are highly similar, whereas those of CH* present a little difference downstream of the flame, probably owing to the processing of chemiluminescence images.

The distributions of OH* and CH* emissions at different heights are further shown in Figure 5, and the simulated and experimental data have been normalized to the maximum of the two. In general, the simulated emissions are close to the experimental data for both OH* and CH*, although the former are a little larger than the latter.

Moreover, as we can see from the two figures, the distribution of CH* is narrower and smaller than that of OH*; in other words, CH* mainly exists closer to the central axis and the burner nozzle. This will be further discussed below.

4.2. Distribution Characteristics of OH* and CH* Radiation. From Figure 6, it is observed that in different zones, the formation of OH* is dominated by different reactions. As shown in Figure 6a, the reaction CH + O_2 = CO + OH* (R4) is intense and is the major channel to generate OH* at a height lower than 5 mm. As the flame spreads downstream, reaction R4 becomes weaker rapidly and the reaction rate of H + O + M = OH* + M (reaction R5) exceeds that of R4 when 20 mm < y < 25 mm, as can be seen in Figure 6b. Then, Figure 6c shows that the major formation pathway of OH* changes to the reaction R5 downstream the flame, as reaction R4 cannot be seen when y > 40 mm. Another interesting finding is that no matter in which area of the flame, the reaction region of reaction R5 is always closer to the flame outer front than that of reaction R4, and it will be further discussed later.

Therefore, the distribution of OH* in the flame can be divided into three groups according to its formation reactions: intense section (I), transition section (II), and secondary section (III), as marked in Figure 7. It is worth noting that this partition is different from the conclusion in He's paper,[3] where they failed to take into account the transition from reactions R4 to R5 and considered zones II and III here as the same regions dominated by reaction R5.

The changes in the concentration of reactants in reactions R4 and R5 from Figure 8 can expound the above findings. Figure 8a reveals that CH, the important reactant of reaction R4, mainly distributes in zone I and almost does not exist at a height of y = 40 mm, which is the main reason that reaction R4 is weak in zone II and negligible in zone III. In addition, the concentration of O_2 also decreases inside the flame front, as illustrated in Figure 8b, but the concentration of O_2 is much larger than that of other reactants, and thus, it may not be a key factor restricting the reaction rate. In contrast, from Figure 8c,d, we can see that the decline of the concentrations of H and O, the reactants of reaction R5, is relatively moderate with the increasing height and they can also be found in zone III. Moreover, the distributions of H and O tend to be external when compared with that of CH. These two points are why the distribution of reaction R5 is closer to the flame front and more extensive.

https://dx.doi.org/10.1021/acsomega.0c01093
ACS Omega 2020, 5, 15922−15930

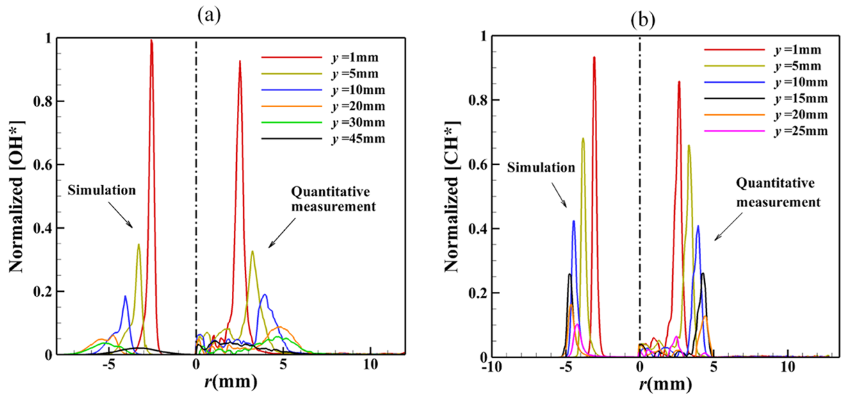

Figure 5. Radial distribution of simulated and measured values of (a) [OH*] and (b) [CH*] at different heights (case 2).

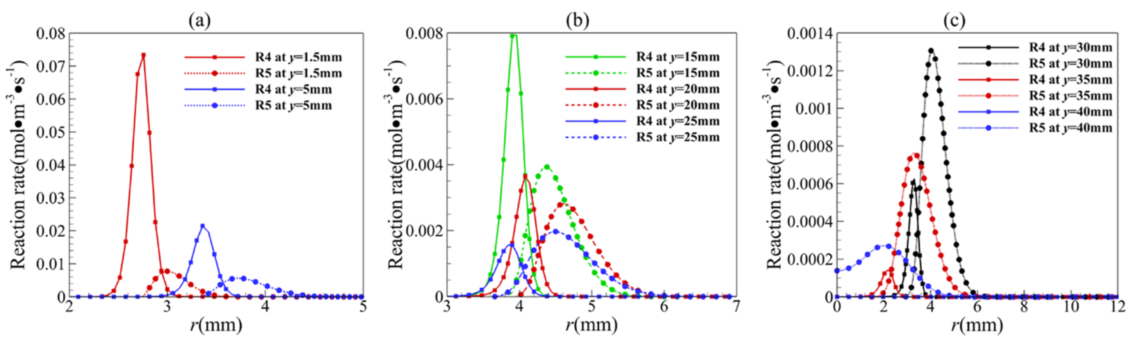

Figure 6. Reaction rate of OH* formation (reactions R4 and R5) at (a) y = 1.5 and 5 mm; (b) y = 15, 20, and 25 mm; and (c) y = 30, 35, and 40 mm.

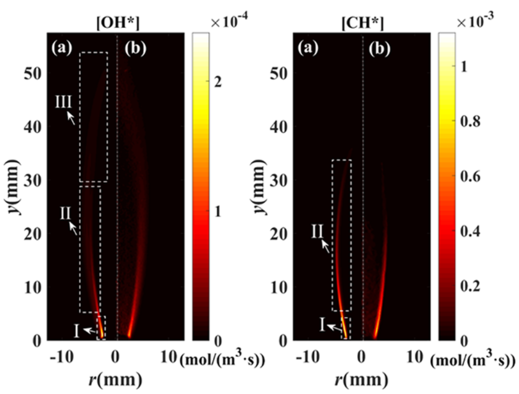

Figure 7. Reaction zone distributions of OH* and CH*: (a) numerical simulation and (b) quantitative measurement (case 2).

By contrast, CH* is distributed in only two regions: intense section (I) and transition section (II), as presented in Figure 7. Besides, from Figure 9a, we can see that reaction C_2H + O = CO + CH* (reaction R15) plays a more important role in the generation of CH* in zone I. Similar to OH*, the reaction rate of C_2H + O_2 = CO_2 + CH* (reaction R14) surpasses that of reaction R15 in the transition section (zone II) as well, as shown in Figure 9b. However, the difference in the reaction rate between reactions R14 and R15 is not as large as reactions R4 and R5. Furthermore, the reaction areas of reactions R4 and R5 are closer to the central axis than those of reactions R14 and R15 and do not exceed r = 5 mm in the radial direction, supporting the narrower distribution of CH* than that of OH*, as observed from Figures 4 and 5.

Figure 8e presents information about the fluctuation in the concentration of C_2H, the important reactant of CH*. As we can see, the concentration of C_2H hits the highest point at the height of y = 5 mm before dropping considerably to almost 0 at y = 35 mm, which explains why CH* has no secondary reaction zone downstream of the flame as OH*. In brief, the CH* distribution is narrower and smaller than that of OH*, suggesting that OH* is more effective in marking the flame structure.

4.3. Effects of k_u on OH* and CH* Radiation. On the basis of the obtained measurements, this section analyzes the impact of increasing airflow velocity on the characteristics of OH* and CH* distributions. The concerned cases 1−5 have gradually improved the exit velocity of air with that of methane unchanged.

The sequence in Figure 10 shows the measurements of OH* and CH* radiation with respect to k_u from 0.2 to 1.0. Due to the symmetry of their distributions, only the right half of each graph was taken for analysis. OH* images have been normalized according to the maximum of the five sets of data, and so are CH* images. It can be seen from the figure that with the increase of k_u, the distribution height of OH* declines and the luminescence of OH* and CH* both become more intense. In addition, the height of OH* is always higher than that of CH* under the same conditions, which is consistent with the phenomenon observed previously.

Figure 11 shows changes in the reactions of OH* and CH* with increasing k_u. Similarly, the data are normalized according to the maximum value of each group. As for the axial distribution of OH*, it can be considered that the peak corresponds to the intense section, the falling section represents the transition zone, and the second smaller peak

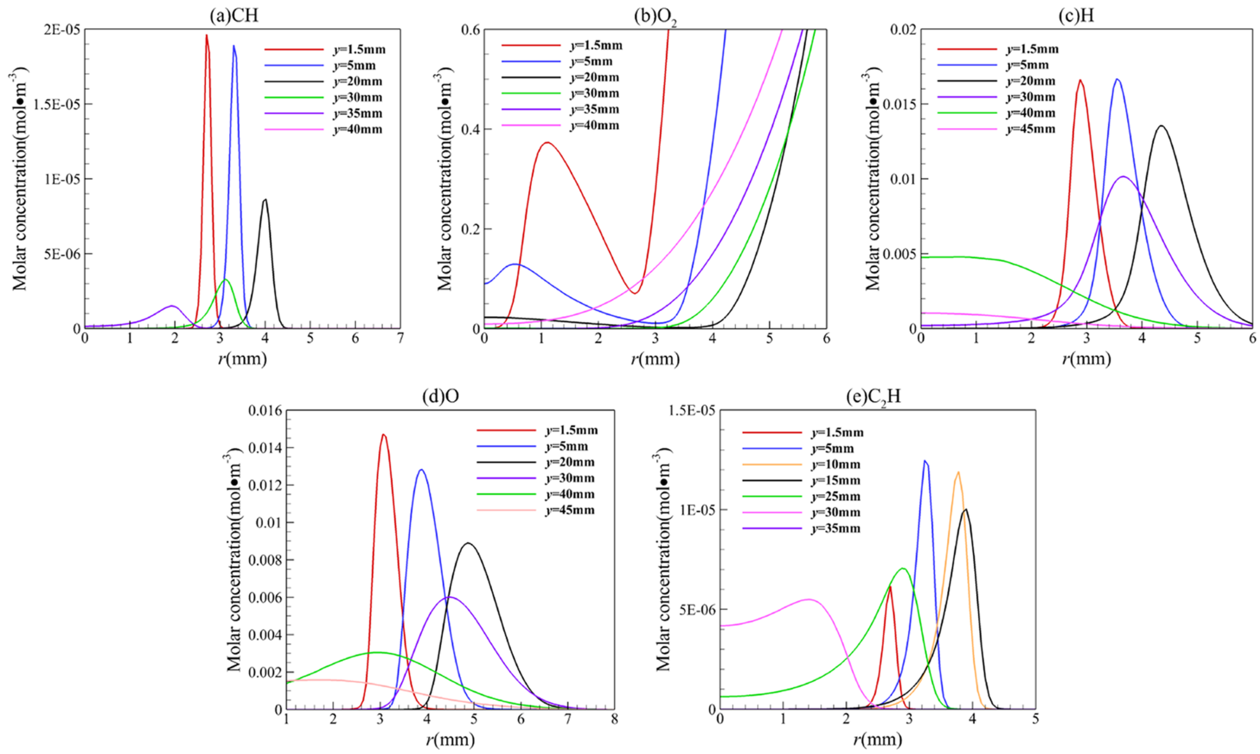

Figure 8. Molar concentration of (a) CH, (b) O_2, (c) H, (d) O, and (e) C_2H at different heights.

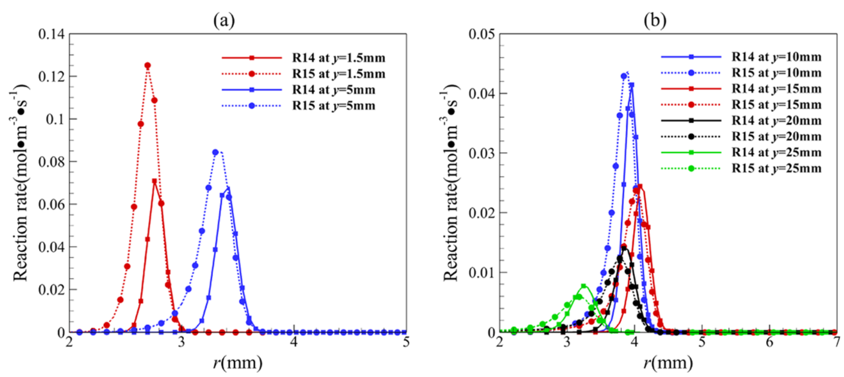

Figure 9. Reaction rate of CH* formation (reactions R14 and R15) at (a) y = 1.5 and 5 mm and (b) y = 10, 15, 20, and 25 mm.

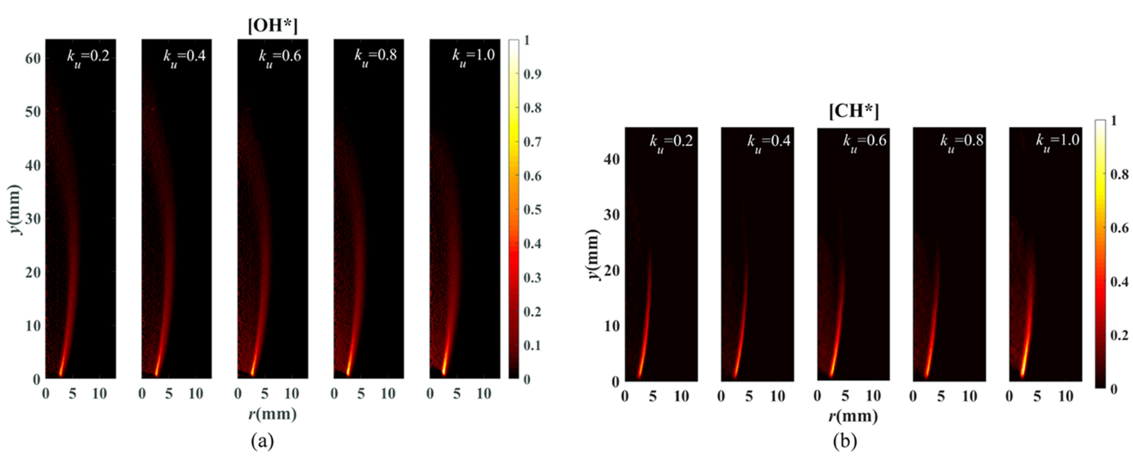

Figure 10. Change in the distributions of (a) [OH*] and (b) [CH*] with different k_u values.

downstream (the black dotted box in Figure 11a) corresponds to the secondary section. As k_u increases, both the axial peaks of OH* and CH* increase, and the peak positions of them develop downstream; while the second peak of OH* decreases.

https://dx.doi.org/10.1021/acsomega.0c01093
ACS Omega 2020, 5, 15922−15930

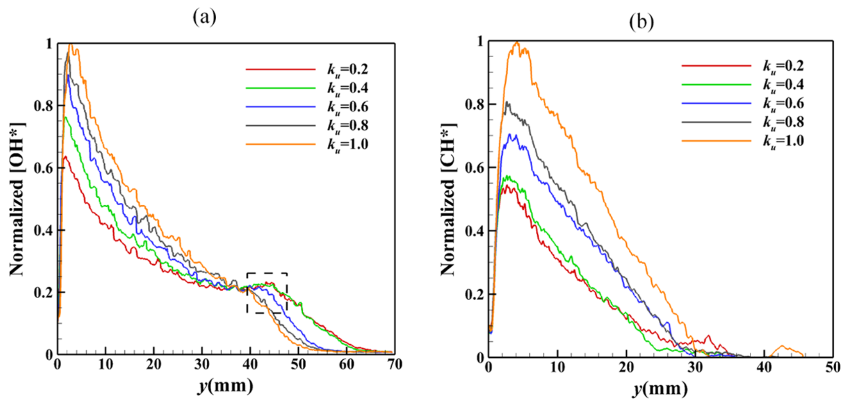

Figure 11. Normalized axial distribution of (a) [OH*] and (b) [CH*] at different $k_u$values.

In other words, the reactions of OH* and CH* in zone I and zone II become more intense with the increasing airflow. Reaction R5, meanwhile, becomes weak in the secondary section (zone III).

5. CONCLUSIONS

A quantitative measurement method of chemiluminescence based on an integrating sphere uniform light source was proposed to realize the transformation of OH* and CH* from the light intensity to the emitting rate in a jet diffusion flame. The experimental measurements agree well with numerical simulation results in distributions and values.

In addition, the more extensive distributions of OH* make it more representative of the flame structure. OH* distributions can be divided into three regions: intense section, transition section, and secondary section, with the dominant production pathway of OH* changing from the reaction CH + O_2 = CO + OH* (R4) to the reaction H + O + M = OH* + M (R5). In contrast, the distribution of CH* is closer to the central axis and the burner nozzle, which can only be found in the first two regions. With the increase of k_u, the main reactions of OH* and CH* become more intense and reaction R5 of OH* in the secondary section becomes weaker.

It is noteworthy that this readily accessible method of chemiluminescence quantification also applies to other axisymmetric flame configurations. More importantly, we believe that it can find future applications in the analysis of chemiluminescence reaction mechanisms and, combined with the 3D CTC technique, it may play a role in bridging the chemiluminescence and combustion characteristics.

■ AUTHOR INFORMATION

Corresponding Author

Jianguo Tan − *College of Aerospace Science and Engineering, National University of Defense Technology, Changsha 410073, Hunan, China;* orcid.org/0000-0003-0083-0779; Email: jianguotan@nudt.edu.cn

Authors

Yao Liu − *College of Aerospace Science and Engineering, National University of Defense Technology, Changsha 410073, Hunan, China;* orcid.org/0000-0001-6173-5738

Minggang Wan − *College of Aerospace Science and Engineering, National University of Defense Technology, Changsha 410073, Hunan, China*

Lang Zhang − *College of Aerospace Science and Engineering, National University of Defense Technology, Changsha 410073, Hunan, China*

Xiao Yao − *College of Aerospace Science and Engineering, National University of Defense Technology, Changsha 410073, Hunan, China*

Complete contact information is available at:
https://pubs.acs.org/10.1021/acsomega.0c01093

Notes

The authors declare no competing financial interest.

■ ACKNOWLEDGMENTS

This work was financially supported by the National Natural Science Foundation of China (91441121).

■ REFERENCES

(1) Zhao, M.; Buttsworth, D.; Choudhury, R. Experimental and numerical study of OH* chemiluminescence in hydrogen diffusion flames. *Combust. Flame* **2018**, *197*, 369−377.

(2) Pan, X.; Yan, W.; Jiang, Y.; Wang, Z.; Hua, M.; Wang, Q.; Jiang, J. Experimental Investigation of the Self-Ignition and Jet Flame of Hydrogen Jets Released under Different Conditions. *ACS Omega* **2019**, *4*, 12004−12011.

(3) He, L.; Guo, Q.; Gong, Y.; Wang, F.; Yu, G. Investigation of OH* chemiluminescence and heat release in laminar methane−oxygen co-flow diffusion flames. *Combust. Flame* **2019**, *201*, 12−22.

(4) Shim, M.; Noh, K.; Yoon, W. Flame structure of methane/oxygen shear coaxial jet with velocity ratio using high-speed imaging and OH*, CH* chemiluminescence. *Acta Astronaut.* **2018**, *147*, 127−132.

(5) Kojima, J.; Ikeda, Y.; Nakajima, T. Basic aspects of OH(A), CH(A), and C2(d) chemiluminescence in the reaction zone of laminar methane−air premixed flames. *Combust. Flame* **2005**, *140*, 34−45.

(6) Song, X.; Guo, Q.; Hu, C.; Gong, Y.; Yu, G. OH* Chemiluminescence Characteristics and Structures of the Impinging Reaction Region in Opposed Impinging Diffusion Flames. *Energy Fuels* **2016**, *30*, 1428−1436.

(7) Deleo, M.; Saveliev, A.; Kennedy, L.; Zelepouga, S. OH and CH luminescence in opposed flow methane oxy-flames. *Combust. Flame* **2007**, *149*, 435−447.

(8) Quintino, F. M.; Trindade, T. P.; Fernandes, E. C. Biogas combustion: Chemiluminescence fingerprint. *Fuel* **2018**, *231*, 328−340.

(9) Lauer, M.; Sattelmayer, T. On the Adequacy of Chemiluminescence as a Measure for Heat Release in Turbulent Flames With Mixture Gradients. *J. Eng. Gas Turbines Power* **2010**, *132*, No. 061502.

(10) Hardalupas, Y.; Orain, M.; Panoutsos, C. S.; Taylor, A. M. K. P.; Olofsson, J.; Seyfried, H.; Richter, M.; Hult, J.; Aldén, M.; Hermann, F.; Klingmann, J. Chemiluminescence sensor for local equivalence ratio of reacting mixtures of fuel and air (FLAMESEEK). *Appl. Therm. Eng.* **2004**, *24*, 1619−1632.

(11) Orain, M.; Hardalupas, Y. Effect of fuel type on equivalence ratio measurements using chemiluminescence in premixed flames. *C. R. Mec.* **2010**, *338*, 241−254.

(12) Zhang, T.; Yu, G.; Guo, Q.; Wang, F. Experimental Study on the Characteristics of Impinging Reaction Region with OH* Chemiluminescence in Opposed Impinging Diffusion Flames. *Energy Fuels* **2013**, *27*, 7023−7030.

(13) Zhang, Q.; Gong, Y.; Guo, Q.; Song, X.; Yu, G. Experimental study on CH* chemiluminescence characteristics of impinging flames in an opposed multi-burner gasifier. *AIChE J.* **2017**, *63*, 2007−2018.

(14) Hardalupas, Y.; Orain, M. Local measurements of the time-dependent heat release rate and equivalence ratio using chemiluminescent emission from a flame. *Combust. Flame* **2004**, *139*, 188−207.

(15) Panoutsos, C. S.; Hardalupas, Y.; Taylor, A. M. K. P. Numerical evaluation of equivalence ratio measurement using OH * and CH * chemiluminescence in premixed and non-premixed methane−air flames. *Combust. Flame* **2009**, *156*, 273−291.

(16) Hardalupas, Y.; Panoutsos, C. S.; Taylor, A. M. K. P. Spatial resolution of a chemiluminescence sensor for local heat-release rate and equivalence ratio measurements in a model gas turbine combustor. *Exp. Fluids* **2010**, *49*, 883−909.

(17) Hossain, A.; Nakamura, Y. A numerical study on the ability to predict the heat release rate using CH* chemiluminescence in non-sooting counterflow diffusion flames. *Combust. Flame* **2014**, *161*, 162−172.

(18) Liu, Y.; Tan, J.; Wang, H.; Lv, L. Characterization of heat release rate by OH* and CH* chemiluminescence. *Acta Astronaut.* **2019**, *154*, 44−51.

(19) Hu, Y.; Tan, J.; Lv, L.; Li, X. Investigations on quantitative measurement of heat release rate using chemiluminescence in premixed methane-air flames. *Acta Astronaut.* **2019**, *164*, 277−286.

(20) Lv, L.; Tan, J.; Zhu, J. Visualization of the heat release zone of highly turbulent premixed jet flames. *Acta Astronaut.* **2017**, *139*, 258−265.

(21) Liu, H.; Wang, Y.; Yu, T.; Liu, H.; Cai, W.; Weng, S. Effect of carbon dioxide content in biogas on turbulent combustion in the combustor of micro gas turbine. *Renewable Energy* **2020**, *147*, 1299−1311.

(22) Zhao, J.; Liu, H.; Cai, W. Numerical and experimental validation of a single-camera 3D velocimetry based on endoscopic tomography. *Appl. Opt.* **2019**, *58*, 1363−1373.

(23) Yu, T.; Cai, W. Simultaneous reconstruction of temperature and velocity fields using nonlinear acoustic tomography. *Appl. Phys. Lett.* **2019**, *115*, No. 104104.

(24) Wang, Q.; Legros, G.; Morin, C.; Yao, M.; Cai, W.; Jiang, L. Optical measurements of temperature fields in sooting flames: influence of soot self-absorption. *Appl. Phys. B* **2019**, *125*, No. 63.

(25) Liu, H.; Paolillo, G.; Astarita, T.; Shui, C.; Cai, W. Computed tomography of chemiluminescence for the measurements of flames confined within a cylindrical glass. *Opt. Lett.* **2019**, *44*, 4793−4796.

(26) Cai, W.; Li, X.; Li, F.; Ma, L. Numerical and experimental validation of a three-dimensional combustion diagnostic based on tomographic chemiluminescence. *Opt. Express* **2013**, *21*, 7050−7064.

(27) Yu, T.; Liu, H.; Cai, W. On the quantification of spatial resolution for three-dimensional computed tomography of chemiluminescence. *Opt. Express* **2017**, *25*, 24093−24108.

(28) Wang, K.; Li, F.; Zeng, H.; Yu, X. Three-dimensional flame measurements with large field angle. *Opt. Express* **2017**, *25*, 21008−21018.

(29) Jin, Y.; Song, Y.; Qu, X.; Li, Z.; Ji, Y.; He, A. Three-dimensional dynamic measurements of CH* and C2* concentrations in flame using simultaneous chemiluminescence tomography. *Opt. Express* **2017**, *25*, 4640−4654.

(30) Wiseman, S. M.; Brear, M. J.; Gordon, R. L.; Marusic, I. Measurements from flame chemiluminescence tomography of forced laminar premixed propane flame. *Combust. Flame* **2017**, *183*, 1−14.

(31) Smith, G. P.; Luque, J.; Park, C.; Jeffries, J. B.; Crosley, D. R. Low pressure flame determinations of rate constants for OH(A) and CH(A) chemiluminescence. *Combust. Flame* **2002**, *131*, 59−69.

(32) Giassi, D.; Cao, S.; Bennett, B. A. V.; Stocker, D. P.; Takahashi, F.; Smooke, M. D.; Long, M. B. Analysis of CH * concentration and flame heat release rate in laminar coflow diffusion flames under microgravity and normal gravity. *Combust. Flame* **2016**, *167*, 198−206.

(33) Nori, V. N.; Seitzman, J. M. CH* chemiluminescence modeling for combustion diagnostics. *Proc. Combust. Inst.* **2009**, *32*, 895−903.

(34) Cao, S.; Ma, B.; Bennett, B. A. V.; Giassi, D.; Stocker, D. P.; Takahashi, F.; Long, M. B.; Smooke, M. D. A computational and experimental study of coflow laminar methane/air diffusion flames: Effects of fuel dilution, inlet velocity, and gravity. *Proc. Combust. Inst.* **2015**, *35*, 897−903.

(35) Wang, K.; Li, F.; Wu, Y.; Yu, X. Quantitative Measurements of Chemiluminescence in a Laminar Methane−Air Premixed Flame and Comparison to Numerical Methods. *Energy Fuels* **2018**, *32*, 5536−5543.

(36) Karnani, S.; Dunn-Rankin, D. Visualizing CH* chemiluminescence in sooting flames. *Combust. Flame* **2013**, *160*, 2275−2278.

(37) Cho, Y. T.; Na, S. J. Application of Abel inversion in real-time calculations for circularly and elliptically symmetric radiation sources. *Meas. Sci. Technol.* **2005**, *16*, 878−884.

(38) Carl, S. A.; Van Poppel, M.; Peeters, J. Identification of the CH + O_2 → OH(A) + CO Reaction as the Source of OH(A−X) Chemiluminescence in $C_2H_2/O/H/O_2$ Atomic Flames and Determination of Its Absolute Rate Constant over the Range T = 296 to 511 K. *J. Phys. Chem. A* **2003**, *107*, 11001−11007.

(39) Tamura, M.; Berg, P. A.; Harrington, J. E.; Luque, J.; Jeffries, J. B.; Smith, G. P.; Crosley, D. R. Collisional Quenching of CH(A), OH(A), and NO(A) in Low Pressure Hydrocarbon Flames. *Combust. Flame* **1998**, *114*, 502−514.

(40) Elsamra, R. M. I.; Vranckx, S.; Carl, S. A. CH($A^2\Delta$) Formation in Hydrocarbon Combustion: The Temperature Dependence of the Rate Constant of the Reaction $C_2H + O_2 \rightarrow CH(A^2\Delta) + CO_2$. *J. Phys. Chem. A* **2005**, *109*, 10287.

https://dx.doi.org/10.1021/acsomega.0c01093
ACS Omega 2020, 5, 15922−15930